NANO LETTERS

pubs.acs.org/NanoLett Letter

Realization of an Antiferromagnetic Superatomic Graphene: Dirac Mott Insulator and Circular Dichroism Hall Effect

Yinong Zhou and Feng Liu*

Cite This: *Nano Lett.* 2021, 21, 230−235 Read Online

ACCESS | Metrics & More | Article Recommendations

ABSTRACT: Using first-principles calculations, we investigate the electronic and topological properties of an antiferromagnetic (AFM) superatomic graphene lattice superimposed on a bipartite honeycomb lattice governed by Lieb's theorem of itinerant magnetism. It affords a concrete material realization of the AFM honeycomb model with a Dirac Mott insulating state, characterized by a gap opening at the Dirac point due to inversion symmetry breaking by long-range AFM order. The opposite Berry curvatures of the K and K' valleys induces a circular dichroism (CD) Hall effect. Different from the valley Hall effect that activates only one valley, the CD Hall effect activates carriers from both K and K' valleys, generating the opposite directions of transversal Hall currents for the left- and right-handed circularly polarized light, respectively.

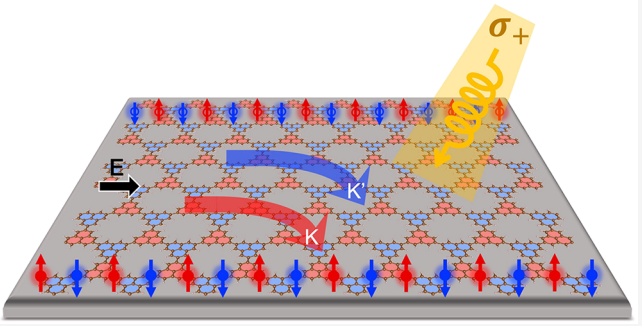

KEYWORDS: *graphene, antiferromagnetic, Mott insulator, circular dichroism Hall effect*

Since 2004, when the first single-layer graphene was extracted from the bulk graphite,[1] graphene has become the most attractive 2D material for fundamental studies, e.g., as a prototypical material of honeycomb lattice model, and practical applications. Beyond graphene, a series of nanostructured graphene superstructures have been proposed and explored, such as graphene nanoribbon,[2−7] nanodots,[8−11] nanoholes,[12,13] and nanoflakes.[14−16] The zigzag edges of graphene-based nanostructures not only show the local magnetism arising from the localized edge states,[3,17,18] but also exhibit long-range magnetic order governed by the Lieb's theorem.[19] By controlling the angle of the zigzag edges, a unified geometric rule was introduced to design graphene-based magnetic nanostructures. In general, two zigzag edges are ferromagnetically and antiferromagnetically coupled when they are at 0 or 120° and 60 or 180°, respectively.[20] The AFM states on a honeycomb lattice have been well studied by the Kane−Mele−Hubbard model.[21−24] The enhancement of the Coulomb repulsion (U) at half-filling leads to phase transitions from a semimetal to a quantum spin liquid then to an AFM Mott insulator in the absence of spin−orbit coupling (SOC). A few materials have been proposed to realize 2D honeycomb lattice with strong electron correlation,[25−29] and graphene does not meet the $U \gg t$ condition for reaching the AFM Mott insulating phase, where t represents the hopping integral. However, it is known that one way to enhance U in graphene is by introducing zigzag edges with highly localized edge states at the Fermi level, which in turn leads to the magnetic order governed by the Lieb's theorem, such as AFM graphene nanoribbons with zigzag edges.[3,6,7] Here, we exploit this strategy to create an AFM superatomic graphene.

On the other hand, in two-dimensional (2D) honeycomb lattice, such as graphene and monolayer transition metal dichalcogenides (TMDs), the electrons display contrasting properties in the two valleys (K and K' at the boundary of the Brillouin zone), which dominate the conductivity. Under time-reversal symmetry, K and K' valleys have opposite Berry curvatures and orbital magnetic moments.[30] This introduces a valley degree of freedom beside the spin and charge degree of freedoms, opening up a new field of valleytronics.[31−36] By breaking inversion symmetry, the carriers of K and K' valleys flow in opposite directions when applying an in-plane electric field, which induces a valley Hall effect.[30,32,33,35−40] The most common way to break inversion symmetry is by considering an on-site energy difference for the bipartite honeycomb lattice, such as the case of the group-VI TMDs.[33,34,38−43] Another way to break inversion symmetry is by invoking the antiferromagnetic (AFM) order, as described by the AFM honeycomb model.[44] Because of the coupling between the valley degree of freedom and AFM order, the underlying degree of freedom

Received: September 4, 2020
Revised: November 6, 2020
Published: December 2, 2020

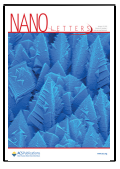

https://dx.doi.org/10.1021/acs.nanolett.0c03579
Nano Lett. 2021, 21, 230−235

becomes the product of spin and valley indices. As a result, an emergent circular dichroism (CD) Hall effect has been proposed,[44] where the direction of transversal Hall current can be controlled by the handedness of the circularly polarized light (CPL).

Using first-principles calculations, we propose a 2D superatomic graphene with an AFM Mott insulating state, as an ideal material realization of the AFM honeycomb model, i.e., Kane-Mele-Hubbard model without SOC, yet without magnetic elements. Each honeycomb site is occupied by a magnetic superatom made of a triangular graphene flake with three ferromagnetic (FM) zigzag edges, whereas the A- and B-site superatoms are antiferromagnetically coupled. In particular, we discuss its topological properties in the context of CD Hall effect for the potential applications of spintronic device.

Our first-principles calculations are performed with the projector-augmented wave pseudopotentials[45,46] and the generalized gradient approximation of Perdew−Burke−Ernzerhof[47] using Vienna Ab initio Simulation Package[48] code. An energy cutoff of 450 eV and a 8 × 8 × 1 Monkhorst−Pack k-point grid is used.[49] The structure is optimized until the atomic forces are smaller than 0.01 eV/Å. The vacuum layer is 15 Å thick to ensure decoupling between neighboring slabs. The antiferromagnetism are considered in the self-consistent calculation.[50] Berry curvatures are calculated by Wannier functions using carbon p_z orbitals.[51,52]

Figure 1a shows the lattice structure of superatomic graphene, which can be potentially fabricated by either a top-down approach of nanopatterning a graphene sheet or a bottom-up approach of self-assembling from molecular graphene precursors. It is essentially a "superatomic" graphene, which replaces each carbon atom in graphene by a "superatom". The superatom is made of a triangular molecular graphene flake consisting of 13 carbon atoms and have exclusively zigzag edges. As such, each superatom is naturally an effective magnetic "element" because its three edges are ferromagnetically coupled at 120° with respect to each other.[20] On other hand, the A-site and B-site superatom are rotated by 60° or 180° relative to each other so that they are antiferromagnetically coupled according to Lieb's theorem of a bipartite lattice.[20] So, in essence, one can view the structure as a superatomic hexagonal lattice superimposed on an atomic hexagonal lattice, and the latter dictates the AFM order of the former. Our first-principles calculations indeed confirm the AFM ground state.[12,20] Without magnetization, two isolated Dirac bands are formed at the Fermi level contributed by the superatomic p_z orbitals, as shown in Figure 1c. Using the density functional theory (DFT) calculations, we find that the energy of the AFM state is 0.11 eV lower than the FM state and 0.12 eV lower than the nonmagnetic state, respectively. On the basis of these energies, we estimate the Néel temperature (T_N) in the Heisenberg model within the mean-field approximation (MFA):[53,54] $\gamma k_B T_N/2 = E_{FM} - E_{AFM}$, where γ is the dimension, k_B is the Boltzmann constant, and E_{FM} and E_{AFM} are the energies of FM and AFM states, respectively. T_N = 213 and 319 K when our system is respectively treated as 3D and 2D. For comparison, the Curie temperature of magnetic semihydrogenated graphene sheet gives 278 and 417 K when it is respectively treated as 3D and 2D.[53] Note that MFA may overestimate the transition temperature. The spin density of the AFM state is shown in Figure 1b. The left/right island can be seen as a spin-up/down superatom forming the AFM honeycomb model. The total magnetic moment for left/right superatom is $\pm 0.472\mu_B$. A large band gap is opened at the Dirac point (K and K' points in the reciprocal lattice) due to the strong Coulomb repulsion, as shown in Figure 1d.

To better understand the AFM band structures, we reproduce the AFM Mott state by a tight-binding model in a honeycomb lattice and compare the band structures with DFT results. The Hamiltonian can be written as

$$H = -t \sum_{\langle ij\rangle\alpha} (c^{\dagger}_{i\alpha} c_{j\alpha} + c^{\dagger}_{j\alpha} c_{i\alpha}) + U \sum_{i} n_{i\uparrow} n_{i\downarrow} \quad (1)$$

$c^{\dagger}_{i\alpha}$ ($c_{i\alpha}$) is the electron creation (annihilation) operator on site i of spin α, and similar for site j. The first term represents the nearest-neighbor hopping (t). The second term represents the on-site electron repulsion of strength U. $n_{i\alpha} = c^{\dagger}_{i\alpha} c_{i\alpha}$ represents the spin-density operator. The schematic lattice model is shown in Figure 2a. The DFT results can be well fitted by this TB model with the parameters of t = 0.1 eV, U = 0.63 eV, as shown in Figure 2b, indicating that superatomic graphene is an

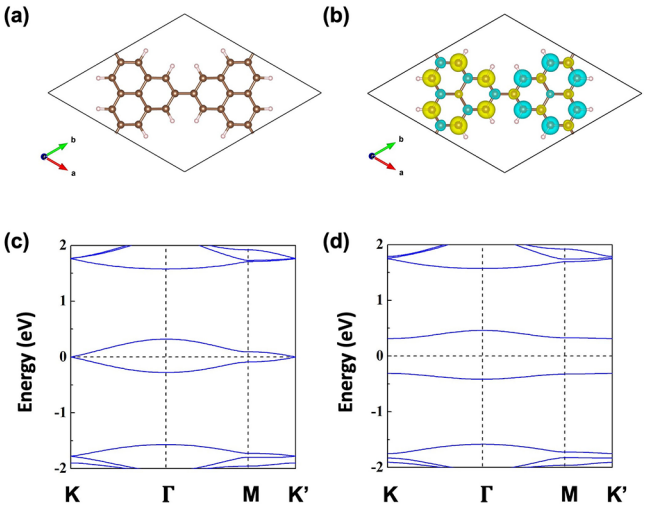

Figure 1. Atomic and band structures of the superatomic graphene. (a) Lattice structure of the superatomic graphene, where the brown spheres represent carbon atoms and the pink spheres represent hydrogen atoms. (b) Spatial distribution of the spin density difference $[\rho_{up}(r) - \rho_{down}(r)]/2$ of the AFM state, where the yellow and blue represent the positive and negative isosurfaces (isovalue = 0.0029/Å^3). (c, d) The band structures for the (c) nonmagnetic and (d) AFM states.

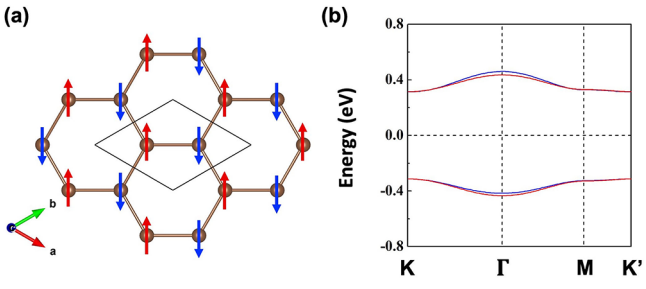

Figure 2. AFM honeycomb model. (a) Schematic diagram of the AFM honeycomb model. The red-up/blue-down arrows represent the spin-up/down. (b) Corresponding band structures, where the red bands are calculated by TB model and the blue bands are calculated by DFT of the superatomic graphene.

https://dx.doi.org/10.1021/acs.nanolett.0c03579
Nano Lett. 2021, 21, 230−235

ideal realization of the AFM honeycomb model in a Mott insulating state of large $U/t = 6.3$ limit.[21]

In a honeycomb lattice, the single orbital hopping gives rise to the half-filled Dirac states with Fermi level located at the K (or K') point in the Brillouin zone, as shown in the middle two bands of Figure 1c, which can be expressed as when $k = K + q$ and $|q| \ll |K|$, $E_{\pm}(q) \approx \pm v_F|q| + O((q/K)^2)$, where the Fermi velocity $v_F = \sqrt{3}ta/2$ when only nearest-neighbor hopping t is considered, and a is the lattice constant.[55] Fundamentally, the Hubbard model is determined by the competition between the Coulomb repulsion (U) and the kinetic energy.[56] Conventionally, the kinetic energy can be represented by hopping integral t or bandwidth W, which is why original Mott insulators are proposed for systems with localized d and f orbitals or with flat bands, such as in twisted bilayer graphene.[25,26] However, in Dirac states, the kinetic energy is proportional to the slope of the linear dispersive bands, i.e., $\sqrt{3}t/2$, independent of bandwidth. That means the bandwidth is no longer a good measure of the kinetic energy of the Dirac states so that Mott transition can happen for large bandwidth, which is $6t$ for Dirac bands in a hexagonal lattice. Here, specifically, the bandwidth is 0.6 eV without considering Coulomb repulsion in Figure 1c, which is comparable with U (0.63 eV). But the condition of $U \gg t$ ($U/t > 4.3$) is still met for Mott transition.[21]

Next, we calculate the Berry curvatures for the gapped valence Dirac band (VDB) and conduction Dirac band (CDB) in Figure 2b for spin-up/down bands of the superatomic graphene using the Wannier functions,[51,52] as shown in Figure 3. For each band, K and K' valleys always have opposite Berry

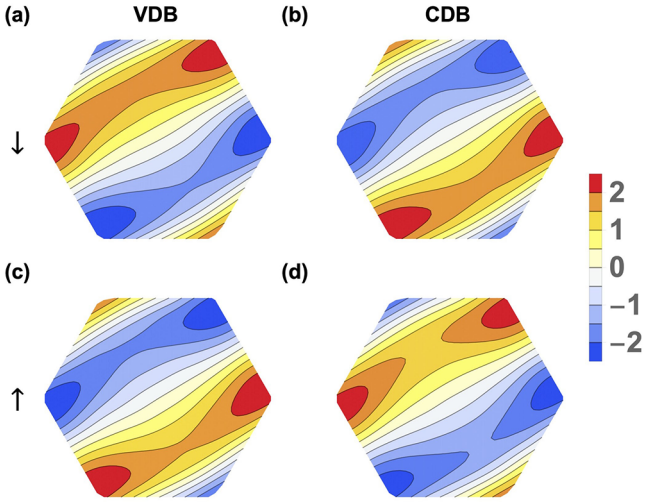

Figure 3. Berry curvatures of the (a) spin-down valence Dirac band (VDB), (b) spin-down conduction Dirac band (CDB), (c) spin-up VDB, (d) spin-up CDB, of the gapped Dirac bands in Figure 2b. The hexagonal region represents the first Brillouin zone.

curvatures. For different spins of the same band, the Berry curvatures are also opposite for the same k (compare Figure 3a, c or Figure 3b, d). In addition, for the same spin at the same k, the Berry curvatures are opposite for the VDB and CDB (compare Figure 3a, b or Figure 3c, d). Note that the total Chern number for each band is zero. All these are consistent with the previous analysis.[30,32−34]

As a result of the opposite Berry curvatures for different spins and valleys, the superatomic graphene exhibits an interesting photoexcitation. As shown in Figure 4a, if a left-

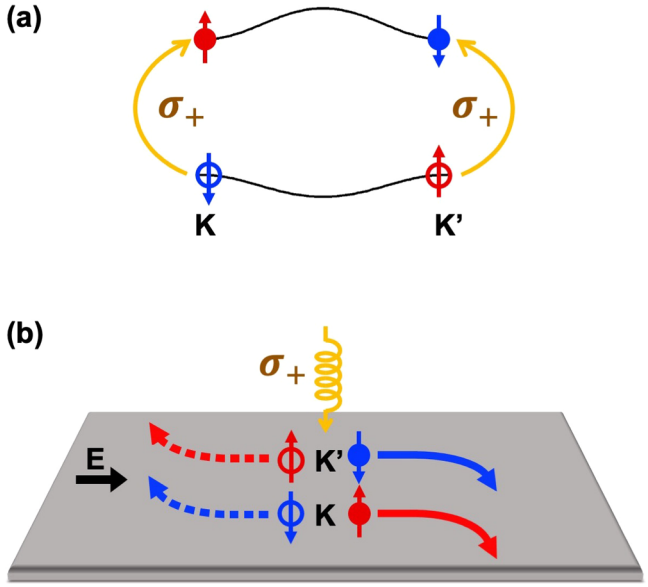

Figure 4. Schematic illustration of circular dichroism (CD) Hall effect. (a) Schematic illustration of left-handed CPL (σ_+) excited electron states of the superatomic graphene. The spin-up/down electron is excited to the CDB in the K/K' valley, and the spin-down/up hole is left on the VDB. (b) CD Hall effect of electrons and holes excited by σ_+. Spin-up/down electrons from the valley K/K' accumulate at the bottom edge.

handed CPL (σ_+) is applied on the material, the spin-up electron is excited to the CDB at K valley, and the spin-down hole is left behind at VDB. At the same time, the spin-down electron is excited to the CDB at K′ valley, and the spin-up hole is left behind at VDB. So, the 1/2-charge carriers are generated, contributing to the conductivity of the so-called CD Hall effect, and the reverse is true for the right-handed CPL (σ_-). Figure 4b shows the CD Hall effect excited by σ_+,[44] where the spin-up electrons from the K valley and spin-down electrons from the K' valley are accumulated at the bottom edge, and the spin-down holes from the K valley and spin-up holes from the K' valley are accumulated at the top edge. For σ_-, the spin-down electrons from the K valley and the spin-up electrons from the K' valley are accumulated at the top edge, and the spin-up holes from K valley and spin-down holes from the K' valley are accumulated at the bottom edge.

We further calculate the interband optical absorption from VDB to CDB for both σ_+ and σ_- CPL. The optical coefficient $\alpha(k)$ is given by[32,57,58]

$$\alpha^{\pm}(k) = \frac{\alpha_0}{E_c(k) - E_v(k)} \sum_{v,c} |\mathcal{P}_x^{cv}(k) \pm i\mathcal{P}_y^{cv}(k)|^2 \quad (2)$$

where $\mathcal{P}_{x,y}^{cv}(k)$ is the electric dipole matrix element $\mathcal{P}_{x,y}^{cv}(k) = \langle \psi_c(k)|\nabla_{x,y}H(k)|\psi_v(k)\rangle$. $E_c(k)$, $E_v(k)$ and $|\Psi_c(k)\rangle, |\Psi_v(k)\rangle$ are eigenvalues and eigenstates for the conduction and valence bands, respectively. $\alpha_0 = e^2/4\pi\varepsilon_0 c\hbar$, where e is the electron charge; ε_0 is the vacuum permittivity; c is the speed of light; and $\hbar$ is the reduced Planck constant. The dissymmetry factor (g), which describes the degree of CD, can be expressed as $g = (\alpha^+ - \alpha^-)/[1/2(\alpha^+ + \alpha^-)]$. Figure 5 shows

https://dx.doi.org/10.1021/acs.nanolett.0c03579
Nano Lett. 2021, 21, 230−235

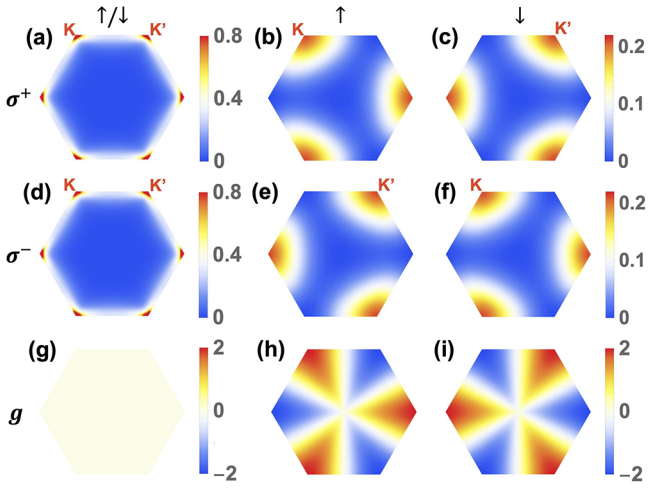

Figure 5. Interband absorbance distributions of (a–c) σ_+ and (d–f) σ_- CPL, and the corresponding distributions of (g–i) g in the first Brillouin zone for different U. (a, d, g) $U = 0$ for spin-up or -down bands, (b, e, h) $U = 6.3t_1$ for spin-up bands, (c, f, i) $U = 6.3t_1$ for spin-down bands, respectively.

the k-space distributions of the absorbance for σ_+ and σ_- CPL and the corresponding distributions of g factor. When $U = 0$, the absorption for K and K′ are the same for σ_+ and σ_- CPL (Figure 5a, d), and the g value equals to zero (Figure 5g). In contrast, when $U = 6.3t_1$, σ_+ CPL excites only spin-up electrons at K and spin-down electrons at K' (Figure 5b,c), which is consistent with the schematic illustration in Figure 4a. Conversely, σ_- CPL excites only spin-up electrons at K' and spin-down electrons at K (Figure 5e, f). The corresponding g value is maximum versus minimum at the K and K' points (Figure 5h, i).

The valley Hall conductivity for K and K' valleys and the total charge Hall conductivity are shown in Table 1. Because

Table 1. Circularly Polarized Light (σ_+ and σ_-)-Induced Valley (K and K') and Charge Hall Effect[a]

polarization		σ_v^K	$\sigma_v^{K'}$	σ
σ_+	e	$(e^2/\hbar)\Omega_K^{\uparrow}$	$(e^2/\hbar)\Omega_{K'}^{\downarrow}$	$2(e^2/\hbar)\Omega$
	h	$(e^2/\hbar)\Omega_K^{\downarrow}$	$(e^2/\hbar)\Omega_{K'}^{\uparrow}$	
σ_-	e	$(e^2/\hbar)\Omega_K^{\downarrow}$	$(e^2/\hbar)\Omega_{K'}^{\uparrow}$	$-2(e^2/\hbar)\Omega$
	h	$(e^2/\hbar)\Omega_K^{\uparrow}$	$(e^2/\hbar)\Omega_{K'}^{\downarrow}$	

[a] σ_v^K and $\sigma_v^{K'}$ represent the valley Hall conductivity for K and K′ valleys, respectively. σ represents the total charge Hall conductivity. e and h denote the electron and hole, respectively. The Berry curvatures $\Omega_K^{\uparrow} = \Omega_{K'}^{\downarrow} = \Omega = -\Omega_K^{\downarrow} = -\Omega_{K'}^{\uparrow}$.

the valley Hall conductivity for K and K' valleys have the same sign, the total charge Hall conductivity is two times of the valley Hall conductivity. σ_+ and σ_- CPL induce the opposite sign of the Hall conductivity. Via controlling the handedness of the CPL, one can easily change the direction of the Hall current.

Lastly, we compare the CD Hall effect in the superatomic graphene and the valley Hall effect in the TMDs. In TMDs, the chirality for spin-up and -down states in one valley are the same; however, they are opposite in the superatomic graphene. Accordingly, in TMDs, σ_+ only excites the electron in K valley, while σ_- only excites the electron in K′ valley; differently, both K and K′ valleys are excited for σ_+ or σ_- CPL in the superatomic graphene. Furthermore, the spin–orbit coupling in TMDs split the spin degeneracy of the valence bands. So, one has to use different frequencies to excite different spin of electrons. As a result, the charge Hall effect in TMDs only exists when both σ_+ and σ_- are applied. And this charge Hall current in TMDs is very small because of the cancellation of electron and hole currents.[33] However, in the superatomic graphene, the charge Hall current is two times of the valley Hall current. The handedness of CPL can easily change the direction of the charge Hall current.

In conclusion, we propose a superatomic graphene with the AFM Mott insulating state governed by the Lieb's theorem, as an ideal realization of the AFM honeycomb model. The Berry curvatures are opposite for different valleys, spins, and valence/conduction Dirac band, induced by the coupling of spin and valley degree of freedom. This unique chirality leads to a CD Hall effect excited by CPL, which can easily change the direction of the Hall current. Our findings enrich the applications of the graphene-based nanostructures and propose a material to realize the CD Hall effect.

AUTHOR INFORMATION

Corresponding Author

Feng Liu – *Department of Materials Science and Engineering, University of Utah, Salt Lake City, Utah 84112, United States;* orcid.org/0000-0002-3701-8058; Email: fliu@eng.utah.edu

Author

Yinong Zhou – *Department of Materials Science and Engineering, University of Utah, Salt Lake City, Utah 84112, United States;* orcid.org/0000-0002-4427-0032

Complete contact information is available at: https://pubs.acs.org/10.1021/acs.nanolett.0c03579

Notes

The authors declare no competing financial interest.

ACKNOWLEDGMENTS

This work is supported by US Department of Energy-Basic Energy Sciences (Grant DE-FG02-04ER46148). The calculations were done on the CHPC at the University of Utah and DOE-NERSC.

REFERENCES

(1) Novoselov, K. S.; Geim, A. K.; Morozov, S. V.; Jiang, D.; Zhang, Y.; Dubonos, S. V.; Grigorieva, I. V.; Firsov, A. A. Electric field effect in atomically thin carbon films. *Science* **2004**, *306*, 666–669.

(2) Kusakabe, K.; Maruyama, M. Magnetic nanographite. *Phys. Rev. B: Condens. Matter Mater. Phys.* **2003**, *67*, 092406.

(3) Son, Y.-W.; Cohen, M. L.; Louie, S. G. Half-metallic graphene nanoribbons. *Nature* **2006**, *444*, 347–349.

(4) Pisani, L.; Chan, J.; Montanari, B.; Harrison, N. Electronic structure and magnetic properties of graphitic ribbons. *Phys. Rev. B: Condens. Matter Mater. Phys.* **2007**, *75*, 064418.

(5) Yan, Q.; Huang, B.; Yu, J.; Zheng, F.; Zang, J.; Wu, J.; Gu, B.-L.; Liu, F.; Duan, W. Intrinsic current- voltage characteristics of graphene nanoribbon transistors and effect of edge doping. *Nano Lett.* **2007**, *7*, 1469–1473.

(6) Huang, B.; Liu, F.; Wu, J.; Gu, B.-L.; Duan, W. Suppression of spin polarization in graphene nanoribbons by edge defects and impurities. *Phys. Rev. B: Condens. Matter Mater. Phys.* **2008**, *77*, 153411.

https://dx.doi.org/10.1021/acs.nanolett.0c03579
Nano Lett. 2021, 21, 230–235

(7) Wang, Z.; Jin, S.; Liu, F. Spatially separated spin carriers in spin-semiconducting graphene nanoribbons. *Phys. Rev. Lett.* **2013**, *111*, 096803.
(8) Ezawa, M. Metallic graphene nanodisks: Electronic and magnetic properties. *Phys. Rev. B: Condens. Matter Mater. Phys.* **2007**, *76*, 245415.
(9) Hod, O.; Barone, V.; Scuseria, G. E. Half-metallic graphene nanodots: A comprehensive first-principles theoretical study. *Phys. Rev. B: Condens. Matter Mater. Phys.* **2008**, *77*, 035411.
(10) Sheng, W.; Luo, K.; Zhou, A. Electric field induced spin polarization in graphene nanodots. *Phys. Rev. B: Condens. Matter Mater. Phys.* **2014**, *90*, 085406.
(11) Tuerhong, M.; Xu, Y.; Yin, X.-B. Review on carbon dots and their applications. *Chinese Journal of Analytical Chemistry* **2017**, *45*, 139−150.
(12) Yu, D.; Lupton, E. M.; Liu, M.; Liu, W.; Liu, F. Collective magnetic behavior of graphene nanohole superlattices. *Nano Res.* **2008**, *1*, 56−62.
(13) Liu, W.; Wang, Z.; Shi, Q.; Yang, J.; Liu, F. Band-gap scaling of graphene nanohole superlattices. *Phys. Rev. B: Condens. Matter Mater. Phys.* **2009**, *80*, 233405.
(14) Fernández-Rossier, J.; Palacios, J. J. Magnetism in graphene nanoislands. *Phys. Rev. Lett.* **2007**, *99*, 177204.
(15) Wang, W. L.; Meng, S.; Kaxiras, E. Graphene nanoflakes with large spin. *Nano Lett.* **2008**, *8*, 241−245.
(16) Wang, W. L.; Yazyev, O. V.; Meng, S.; Kaxiras, E. Topological frustration in graphene nanoflakes: magnetic order and spin logic devices. *Phys. Rev. Lett.* **2009**, *102*, 157201.
(17) Nakada, K.; Fujita, M.; Dresselhaus, G.; Dresselhaus, M. S. Edge state in graphene ribbons: Nanometer size effect and edge shape dependence. *Phys. Rev. B: Condens. Matter Mater. Phys.* **1996**, *54*, 17954.
(18) Fujita, M.; Wakabayashi, K.; Nakada, K.; Kusakabe, K. Peculiar localized state at zigzag graphite edge. *J. Phys. Soc. Jpn.* **1996**, *65*, 1920−1923.
(19) Lieb, E. H. Two theorems on the Hubbard model. *Phys. Rev. Lett.* **1989**, *62*, 1201.
(20) Yu, D.; Lupton, E. M.; Gao, H.; Zhang, C.; Liu, F. A unified geometric rule for designing nanomagnetism in graphene. *Nano Res.* **2008**, *1*, 497−501.
(21) Meng, Z.; Lang, T.; Wessel, S.; Assaad, F.; Muramatsu, A. Quantum spin liquid emerging in two-dimensional correlated Dirac fermions. *Nature* **2010**, *464*, 847−851.
(22) Hohenadler, M.; Lang, T.; Assaad, F. Correlation effects in quantum spin-hall insulators: A quantum monte carlo study. *Phys. Rev. Lett.* **2011**, *106*, 100403.
(23) Zheng, D.; Zhang, G.-M.; Wu, C. Particle-hole symmetry and interaction effects in the Kane-Mele-Hubbard model. *Phys. Rev. B: Condens. Matter Mater. Phys.* **2011**, *84*, 205121.
(24) Hohenadler, M.; Meng, Z.; Lang, T.; Wessel, S.; Muramatsu, A.; Assaad, F. Quantum phase transitions in the Kane-Mele-Hubbard model. *Phys. Rev. B: Condens. Matter Mater. Phys.* **2012**, *85*, 115132.
(25) Cao, Y.; Fatemi, V.; Demir, A.; Fang, S.; Tomarken, S. L.; Luo, J. Y.; Sanchez-Yamagishi, J. D.; Watanabe, K.; Taniguchi, T.; Kaxiras, E.; Ashoori, R. C.; Jarillo-Herrero, P. Correlated insulator behaviour at half-filling in magic-angle graphene superlattices. *Nature* **2018**, *556*, 80−84.
(26) Cao, Y.; Fatemi, V.; Fang, S.; Watanabe, K.; Taniguchi, T.; Kaxiras, E.; Jarillo-Herrero, P. Unconventional superconductivity in magic-angle graphene superlattices. *Nature* **2018**, *556*, 43−50.
(27) Thomas, S.; Li, H.; Bredas, J.-L. Emergence of an Antiferromagnetic Mott Insulating Phase in Hexagonal π-Conjugated Covalent Organic Frameworks. *Adv. Mater.* **2019**, *31*, 1900355.
(28) Luo, M. Antiferromagnetic spin valve based on a hetero-structure of two-dimensional hexagonal crystals. *Phys. Rev. B: Condens. Matter Mater. Phys.* **2019**, *99*, 165407.
(29) Lee, J.; Jin, K.-H.; Catuneanu, A.; Go, A.; Jung, J.; Won, C.; Cheong, S.-W.; Kim, J.; Liu, F.; Kee, H.-Y.; Yeom, H. W. Honeycomb-Lattice Mott insulator on Tantalum Disulphide. *Phys. Rev. Lett.* **2020**, *125*, 096403.
(30) Xiao, D.; Yao, W.; Niu, Q. Valley-contrasting physics in graphene: magnetic moment and topological transport. *Phys. Rev. Lett.* **2007**, *99*, 236809.
(31) Rycerz, A.; Tworzydło, J.; Beenakker, C. Valley filter and valley valve in graphene. *Nat. Phys.* **2007**, *3*, 172.
(32) Yao, W.; Xiao, D.; Niu, Q. Valley-dependent optoelectronics from inversion symmetry breaking. *Phys. Rev. B: Condens. Matter Mater. Phys.* **2008**, *77*, 235406.
(33) Xiao, D.; Liu, G.-B.; Feng, W.; Xu, X.; Yao, W. Coupled spin and valley physics in monolayers of MoS 2 and other group-VI dichalcogenides. *Phys. Rev. Lett.* **2012**, *108*, 196802.
(34) Cao, T.; Wang, G.; Han, W.; Ye, H.; Zhu, C.; Shi, J.; Niu, Q.; Tan, P.; Wang, E.; Liu, B.; Feng, J. Valley-selective circular dichroism of monolayer molybdenum disulphide. *Nat. Commun.* **2012**, *3*, 887.
(35) Gorbachev, R.; Song, J.; Yu, G.; Kretinin, A.; Withers, F.; Cao, Y.; Mishchenko, A.; Grigorieva, I.; Novoselov, K.; Levitov, L.; Geim, A. K. Detecting topological currents in graphene superlattices. *Science* **2014**, *346*, 448−451.
(36) Schaibley, J. R.; Yu, H.; Clark, G.; Rivera, P.; Ross, J. S.; Seyler, K. L.; Yao, W.; Xu, X. Valleytronics in 2D materials. *Nature Reviews Materials* **2016**, *1*, 1−15.
(37) Akhmerov, A.; Beenakker, C. Detection of valley polarization in graphene by a superconducting contact. *Phys. Rev. Lett.* **2007**, *98*, 157003.
(38) Feng, W.; Yao, Y.; Zhu, W.; Zhou, J.; Yao, W.; Xiao, D. Intrinsic spin Hall effect in monolayers of group-VI dichalcogenides: A first-principles study. *Phys. Rev. B: Condens. Matter Mater. Phys.* **2012**, *86*, 165108.
(39) Qi, J.; Li, X.; Niu, Q.; Feng, J. Giant and tunable valley degeneracy splitting in MoTe 2. *Phys. Rev. B: Condens. Matter Mater. Phys.* **2015**, *92*, 121403.
(40) Tong, W.-Y.; Gong, S.-J.; Wan, X.; Duan, C.-G. Concepts of ferrovalley material and anomalous valley Hall effect. *Nat. Commun.* **2016**, *7*, 13612.
(41) Singh, N.; Schwingenschlögl, U. A route to permanent valley polarization in monolayer MoS2. *Adv. Mater.* **2017**, *29*, 1600970.
(42) Zhao, C.; et al. Enhanced valley splitting in monolayer WSe 2 due to magnetic exchange field. *Nat. Nanotechnol.* **2017**, *12*, 757.
(43) Beyer, H.; Rohde, G.; Grubisic Cabo, A.; Stange, A.; Jacobsen, T.; Bignardi, L.; Lizzit, D.; Lacovig, P.; Sanders, C. E.; Lizzit, S.; Rossnagel, K.; Hofmann, P.; Bauer, M. 80% Valley Polarization of Free Carriers in Singly Oriented Single-Layer WS 2 on Au (111). *Phys. Rev. Lett.* **2019**, *123*, 236802.
(44) Li, X.; Cao, T.; Niu, Q.; Shi, J.; Feng, J. Coupling the valley degree of freedom to antiferromagnetic order. *Proc. Natl. Acad. Sci. U. S. A.* **2013**, *110*, 3738−3742.
(45) Blöchl, P. E. Projector augmented-wave method. *Phys. Rev. B: Condens. Matter Mater. Phys.* **1994**, *50*, 17953.
(46) Kresse, G.; Joubert, D. From ultrasoft pseudopotentials to the projector augmented-wave method. *Phys. Rev. B: Condens. Matter Mater. Phys.* **1999**, *59*, 1758.
(47) Perdew, J. P.; Burke, K.; Ernzerhof, M. Generalized gradient approximation made simple. *Phys. Rev. Lett.* **1996**, *77*, 3865.
(48) Kresse, G.; Furthmüller, J. Efficient iterative schemes for ab initio total-energy calculations using a plane-wave basis set. *Phys. Rev. B: Condens. Matter Mater. Phys.* **1996**, *54*, 11169.
(49) Methfessel, M.; Paxton, A. High-precision sampling for Brillouin-zone integration in metals. *Phys. Rev. B: Condens. Matter Mater. Phys.* **1989**, *40*, 3616.
(50) Hobbs, D.; Kresse, G.; Hafner, J. Fully unconstrained noncollinear magnetism within the projector augmented-wave method. *Phys. Rev. B: Condens. Matter Mater. Phys.* **2000**, *62*, 11556.
(51) Marzari, N.; Vanderbilt, D. Maximally localized generalized Wannier functions for composite energy bands. *Phys. Rev. B: Condens. Matter Mater. Phys.* **1997**, *56*, 12847.

https://dx.doi.org/10.1021/acs.nanolett.0c03579
Nano Lett. 2021, 21, 230−235

(52) Wu, Q.; Zhang, S.; Song, H.-F.; Troyer, M.; Soluyanov, A. A. WannierTools: An open-source software package for novel topological materials. *Comput. Phys. Commun.* **2018**, *224*, 405−416.
(53) Zhou, J.; Wang, Q.; Sun, Q.; Chen, X.; Kawazoe, Y.; Jena, P. Ferromagnetism in semihydrogenated graphene sheet. *Nano Lett.* **2009**, *9*, 3867−3870.
(54) Li, L.; Qin, R.; Li, H.; Yu, L.; Liu, Q.; Luo, G.; Gao, Z.; Lu, J. Functionalized graphene for high-performance two-dimensional spintronics devices. *ACS Nano* **2011**, *5*, 2601−2610.
(55) Castro Neto, A. H.; Guinea, F.; Peres, N. M. R.; Novoselov, K. S.; Geim, A. K. The electronic properties of graphene. *Rev. Mod. Phys.* **2009**, *81*, 109−162.
(56) Hubbard, J. Electron correlations in narrow energy bands. *Proc. R. Soc. London, Ser. A* **1963**, *276*, 238−257.
(57) Lew Yan Voon, L. C.; Ram-Mohan, L. R. Tight-binding representation of the optical matrix elements: Theory and applications. *Phys. Rev. B: Condens. Matter Mater. Phys.* **1993**, *47*, 15500.
(58) Graf, M.; Vogl, P. Electromagnetic fields and dielectric response in empirical tight-binding theory. *Phys. Rev. B: Condens. Matter Mater. Phys.* **1995**, *51*, 4940.

https://dx.doi.org/10.1021/acs.nanolett.0c03579
Nano Lett. 2021, 21, 230−235